Available online at www.sciencedirect.com

ScienceDirect

Advances in Space Research 57 (2016) 1440–1447

ADVANCES IN SPACE RESEARCH (a COSPAR publication)

www.elsevier.com/locate/asr

On–off intermittency and spatiotemporal chaos in three-dimensional Rayleigh–Bénard convection

Emanuel V. Chimanski [a,*], Erico L. Rempel [a,b], Roman Chertovskih [a]

[a] Aeronautics Institute of Technology – IEFM/ITA, 12228-900 São José dos Campos, SP, Brazil
[b] National Institute for Space Research – DGE/INPE and World Institute for Space Environment Research – WISER, P.O. Box 515, 12227-010 São José dos Campos, SP, Brazil

Received 6 June 2015; received in revised form 10 November 2015; accepted 19 November 2015
Available online 2 December 2015

Abstract

Convective instabilities of viscous conducting fluids play an important role in many physical phenomena in planets and stars. Astrophysical magnetic fields are usually explained in a framework of the dynamo theory, describing transformation of the kinetic energy of a flow into magnetic energy. Therefore, an analysis of purely convective states and their bifurcations, as a control parameter is changed, provides a detailed framework for the subsequent study of magnetic field generation by these states. In this paper, three-dimensional Rayleigh–Bénard convection in the absence of magnetic field is investigated numerically for various values of the Rayleigh number and a fixed Prandtl number (corresponding to its value for convection in the Earth's outer core). On increasing the Rayleigh number, we identified periodic, quasiperiodic, chaotic and hyperchaotic attractors of the convective system and their bifurcations, thereby describing a route to spatiotemporal chaos in the convective system. The occurrence of on–off intermittency in the energy time series is discussed.

Keywords: Rayleigh–Bénard convection; Hyperchaos; Spatiotemporal chaos

1. Introduction

Thermal convection is one of the most efficient and widespread mechanisms of mass and energy transport in fluids, acting in the terrestrial atmosphere as well as in the interior of planets and stars. Solar convection is responsible for the formation of fluid cells observable as granular patterns in the photosphere (Chian and Kamide, 2007). Convective flows with a strong shear in the solar convection zone are believed to be responsible for intensification of the magnetic flux (Brandenburg and Subramanian, 2005). Efficiency of this amplification mechanism relies on some properties of the velocity field, that should be able to stretch, twist and fold the magnetic field lines in such way that magnetic flux is increased (Childress and Gilbert, 1995). Terrestrial magnetic fields are also generated by convective flows of a conducting fluid in the liquid outer core (Rüdiger and Hollerbach, 2004).

Rayleigh–Bénard (R–B) convection refers to the motion of a viscous fluid in a plane horizontal layer heated from below in a gravitational field with a vertical temperature gradient. It has been extensively studied due to the feasibility of both analytical, numerical and experimental treatments (Chandrasekhar, 1961; Bodenschatz et al., 2000). For over a century, R–B convection has been explored for pattern formation in systems outside of equilibrium (Bénard, 1901; Cross and Hohenberg, 1993). It is also the

* Corresponding author.
E-mail addresses: chimanski@ita.br (E.V. Chimanski), rempel@ita.br (E.L. Rempel), roman@ita.br (R. Chertovskih).

http://dx.doi.org/10.1016/j.asr.2015.11.014
0273-1177/

simplest framework to explain the formation of convective patterns in astro- and geophysics (Fowler, 2005).

Control parameters in R–B convection are the Rayleigh number, R, measuring the magnitude of the thermal buoyancy force, and the Prandtl number, P, the ratio of kinematic viscosity to thermal diffusivity. Values of these parameters identify properties of the convective flow, therefore regions in the two-dimensional parameter space are used to describe instabilities, pattern formation, symmetry breaking and transition to turbulence in convection.

The dynamical systems theory and the bifurcation theory have been used to explain transition to turbulence in the R–B convection since Edward Lorenz's reduced model (Lorenz, 1963). Its chaotic behavior, characterized by irregular time dynamics, sensitivity to initial conditions and presence of a positive Lyapunov exponent, was a first step towards a dynamical systems description of a turbulent flow. The Lyapunov exponents measure the average exponential rate of growth/shrinkage of initially close trajectories in the phase space. Variating a control parameter of a hydrodynamic system towards turbulent flows, one expects the system to become progressively more irregular in time and space, in a state with more than one positive Lyapunov exponent – *hyperchaotic* state (Rössler, 1979). Hyperchaos was found in generalized Lorenz systems (Zhou et al., 2008; Macek and Strumik, 2014). In a more realistic setup, Paul et al. (2011) detected hyperchaos in a reduced model of the R–B convection, for two-dimensional flows and keeping only 14 complex and 2 real Fourier modes of the solution. Hyperchaotic states were also found in studies of spiral defect chaos using simulations of three-dimensional R–B convection in cylindrical domains (Egolf et al., 2000; Paul et al., 2007; Karimi and Paul, 2012). The spectrum of Lyapunov exponents was used *ibid.* to compute the fractal dimension of the underlying convective state, by this means quantifying the extensive spatiotemporal chaos and studying dependence of the number of dynamical degrees of freedom on the size of the system.

In the present paper, results of a study on transition to hyperchaos in R–B convection in hydrodynamics are reported. The Prandtl number is fixed at $P = 0.3$ and the Rayleigh number is varied as a control parameter. This value of P is interesting for the study of the geodynamo, since in the outer core P is estimated to be between 0.1 and 0.5 (Olson, 2007; Fearn and Roberts, 2007). We follow the works by Podvigina (2006, 2008), where several attractors and bifurcations of the convective system in the same range of parameters were identified. The paper is organized as follows. In Section 2, equations governing the convective system, boundary conditions and numerical methods are presented. In Section 3, attractors of the convective system for increasing values of the Rayleigh number are presented and an observed route to spatiotemporal chaos is discussed. Here, we employ the term spatiotemporal chaos to denote hyperchaos in a spatially extended dynamical system. The conclusions are given in Section 4.

2. The model

A newtonian incompressible fluid is confined between two infinite horizontal planes in a square periodic cell $\mathcal{D} = [0, L]^2 \times [0, 1]$, see Fig. 1. The fluid is uniformly heated from below. Temperatures at the bottom, T_1, and the top, T_2, planes are fixed, with $T_1 > T_2$. Under the Boussinesq approximation, considering the vertical size of the fluid container d as a length scale, the vertical heat diffusion time $\tau_v = d^2/\kappa$ as a time scale, and the vertical temperature gradient δT as a temperature scale, the dynamics of three-dimensional R–B convection in a plane layer is governed, in a dimensionless form, by Chandrasekhar (1961) and Getling (1998) the Navier–Stokes equation,

$$\frac{\partial \mathbf{v}}{\partial t} = P\nabla^2 \mathbf{v} + \mathbf{v} \times (\nabla \times \mathbf{v}) + PR\theta \mathbf{e}_z - \nabla p, \tag{1}$$

the heat transfer equation,

$$\frac{\partial \theta}{\partial t} = \nabla^2 \theta - (\mathbf{v} \cdot \nabla)\theta + v_z, \tag{2}$$

and the incompressibility condition,

$$\nabla \cdot \mathbf{v} = 0, \tag{3}$$

where $\mathbf{v}(\mathbf{x}, t)$ is fluid velocity, $p(\mathbf{x}, t)$ the modified pressure and $\theta(\mathbf{x}, t) = T(\mathbf{x}, t) - (T_1 + (T_2 - T_1)z)$ is the difference of the temperature and its linear profile. The dimensionless parameters are the Prandtl number P (representing the material properties of the fluid),

$$P = \frac{\nu}{\kappa},$$

and the Rayleigh number R (representing the magnitude of the buoyancy force),

$$R = \frac{\alpha g \delta T d^3}{\nu \kappa},$$

with g representing the gravitational acceleration, ν, κ and α the kinematic viscosity, thermal diffusivity and thermal expansion coefficients, respectively.

The horizontal boundaries (non-deformable and impermeable by the fluid), defined by $z = 0$ and $z = 1$, are held at constant temperatures,

$$T(\mathbf{x}, t)|_{z=0} = T_1, \quad T(\mathbf{x}, t)|_{z=1} = T_2, \quad T_1 > T_2,$$

i.e.,

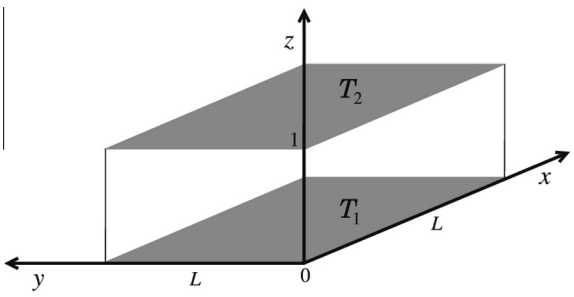

Fig. 1. Computational domain for the horizontal plane layer.

$$\theta(\mathbf{x},t)|_{z=0} = \theta(\mathbf{x},t)|_{z=1} = 0.$$

The fluid flow is stress free on the horizontal boundaries,

$$\frac{\partial v_x}{\partial z} = \frac{\partial v_y}{\partial z} = v_z = 0,$$

and periodicity in the horizontal directions with the same period L is assumed,

$$\mathbf{v}(x,y,z) = \mathbf{v}(x+mL, y+nL, z),$$
$$\theta(x,y,z) = \theta(x+mL, y+nL, z),$$
$$p(x,y,z) = p(x+mL, y+nL, z), \quad \forall m,n \in \mathbb{Z}.$$

Eqs. (1)–(3) are solved numerically by applying the pseudospectral method (Boyd, 2000), in which all fields are represented in the form of truncated Fourier series, e.g., the velocity field,

$$v_j = \sum_{k_x=-N/2+1}^{N/2-1} \sum_{k_y=-N/2+1}^{N/2-1} \sum_{k_z=0}^{N/2} \widehat{v}^j_{k_x,k_y,k_z}(t) e^{2\pi i(k_x x + k_y y)/L} f^j,$$

$$j = x, y, z,$$

where $f^x = f^y = \cos(\pi k_z z)$ and $f^z = \sin(\pi k_z z)$. The vector notation for the Fourier coefficients and wave vectors,

$$\widehat{\mathbf{v}}_{\mathbf{k}} = \left(\widehat{v}^x_{\mathbf{k}}(t), \widehat{v}^y_{\mathbf{k}}(t), \widehat{v}^z_{\mathbf{k}}(t)\right), \quad \mathbf{k} = (k_x, k_y, k_z),$$

is used in what follows. Upon substitution of the series into (1)–(3), the resulting ODEs for the Fourier coefficients are solved by the third-order exponential time differencing method ETDRK3 (Cox and Matthews, 2002) with a constant time step.

3. Results

The convective system is studied for values of the Rayleigh number varying from 1720 to 2500, while the other parameters were fixed: $P = 0.3$ and $L = 4$. We computed the kinetic energy

$$E_v = \frac{1}{L^2} \int_0^L \int_0^L \int_0^1 \frac{1}{2}\mathbf{v}^2 \, d\mathbf{x},$$

and the kinetic energy spectrum,

$$E_v(n) = \sum_{\mathbf{k}\in C_n} \frac{1}{2} |\widehat{\mathbf{v}}_{\mathbf{k}}|^2,$$

where the spherical shells C_n in the Fourier space are defined as

$$C_n = \{\mathbf{k} : n-1 < |\mathbf{k}| \leqslant n\}, \quad n \in \mathbb{N}.$$

Spatial resolution of $32 \times 32 \times 16$ Fourier harmonics was employed (the nonlinear terms were evaluated on a uniform $48 \times 48 \times 25$ grid to eliminate the aliasing error); the kinetic energy spectra for all the attractors decreases at least by 5 orders of magnitude. We checked that doubling the spatial resolution does not significantly affect the solution (see the time-averaged kinetic energy spectra for the velocity field of the attractor at $R = 2500$ shown on Fig. 2).

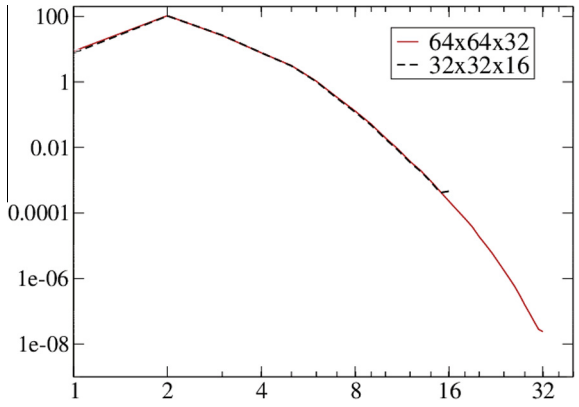

Fig. 2. Time-averaged kinetic energy spectrum, $\langle E_v(n)\rangle$, (vertical axis) of the flow for the hyperchaotic attractor $R = 2500$ computed with spatial resolution of $32 \times 32 \times 16$ (black dotted line) and $64 \times 64 \times 32$ (red solid line) Fourier harmonics. Horizontal axis: spherical shell number, n. (For interpretation of the references to color in this figure legend, the reader is referred to the web version of this article.)

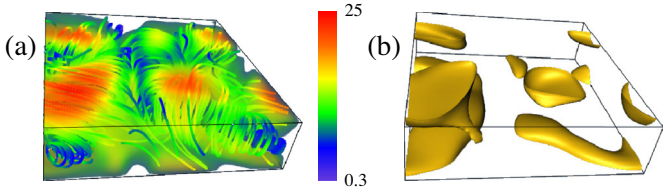

Fig. 3. (a) Snapshot of streamlines and the absolute value of the velocity field and (b) isosurface of the absolute value of the velocity field (defined by isovalue – 17) for the hyperchaotic attractor at $R = 2500$.

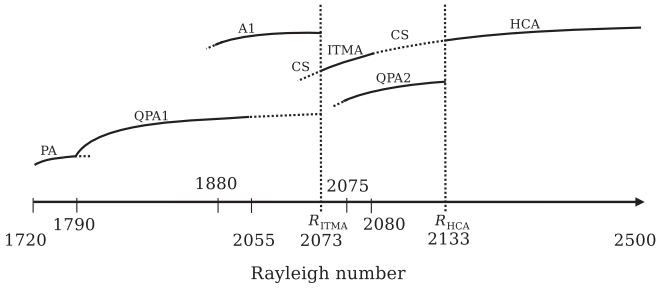

Fig. 4. Bifurcation diagram of attractors found for $1720 \leqslant R \leqslant 2500$. Intervals of existence and values of kinetic energy are given in Table 1.

In the considered range of R, all asymptotically stable solutions (attractors) are of the form of deformed rolls, see e.g., the attractor for $R = 2500$ on Fig. 3.

The convective attractors found are represented on the schematic bifurcation diagram of Fig. 4. The solid lines represent stable convective states and the dashed lines, unstable states. For some intervals in R two attractors of different type coexist, i.e., the asymptotic behavior of a solution depends on the initial conditions. The intervals of R where each attractor appears/disappears, as well as their time-averaged kinetic energy along the intervals is found in Table 1.

To classify the regimes, the three largest Lyapunov exponents $\lambda_1 \geqslant \lambda_2 \geqslant \lambda_3$ were computed by the method

Table 1
Branches of attractors of the convective system for $1720 \leqslant R \leq 2500$. The last column presents the time-averaged kinetic energy.

Label	Type	Interval of existence	$\langle E_v \rangle$
PA	Periodic	$1720 \leqslant R \leqslant 1780$	69–73
QPA1	Quasiperiodic	$1790 \leqslant R \leqslant 2055$	74–91
A1	Quasiperiodic/chaotic	$1880 \leqslant R \leqslant 2070$	89–110
ITMA	Chaotic (intermittent)	$2073 \leqslant R \leqslant 2080$	92–94
QPA2	Quasiperiodic	$2075 \leqslant R \leqslant 2130$	92–99
HCA	Hyperchaotic	$2133 \leqslant R \leqslant 2500$	110–150

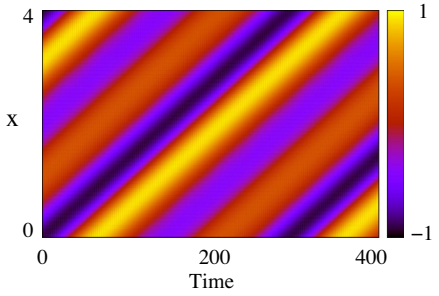

Fig. 5. Space–time evolution of the vertical averages of v_x for the quasiperiodic attractor QPA1 at $R = 1795$.

described in Hramov et al. (2012), using linearization of the governing Eqs. (1)–(3). Positive values of the Lyapunov exponents indicate exponential divergence of nearby initial conditions. In a p-dimensional phase space system, a periodic solution has one vanishing Lyapunov exponent $\lambda_1 = 0$ and $\lambda_i < 0$ for $i = 2, \ldots, p$. For a quasiperiodic solution, there are k vanishing Lyapunov exponents corresponding to k-incommensurate frequencies. For a chaotic attractor, at least one Lyapunov exponent is positive, with the attractor being called hyperchaotic when it has more than one positive exponent (Alligood et al., 1997; Kapitaniak et al., 2000).

For $1720 \leqslant R \leqslant 1780$, the system converges to periodic attractors (PA) that have one vanishing and two negative Lyapunov exponents. On increasing R, PA undergoes a Hopf bifurcation, giving rise to a quasiperiodic attractor, QPA1, constituted by a time-periodic regime drifting with constant speed along a horizontal direction. This can be seen in Fig. 5, where the vertical (yz) averages of v_x are plotted as a function of time, revealing the traveling waves. These states are stable for $1790 \leqslant R \leqslant 2055$ and are characterized by $\lambda_{1,2} = 0$ and $\lambda_3 < 0$.

Fig. 6 shows the evolution of the kinetic energy (left panels), the phase space trajectories of the Fourier coefficient $\widehat{v}^x_{2,1,2}$ (upper right panels) and absolute values, which eliminates drift frequencies, $||\widehat{v}^x_{2,1,2}||$ versus $||\widehat{v}^y_{2,1,2}||$ (bottom right panels) for both PA and QPA1. For Fig. 6(a), the evolution of the kinetic energy and projections of $\widehat{v}^x_{2,1,2}$ ($\mathrm{Re}(\widehat{v}^x_{2,1,2})$,$\mathrm{Im}(\widehat{v}^x_{2,1,2})$) are periodic in time. A closed curve is observed (right-bottom panel) for the periodic attractor PA. The energy time series of QPA1 (left panel in Fig. 6 (b)) masks the quasiperiodicity of the attractor but a torus

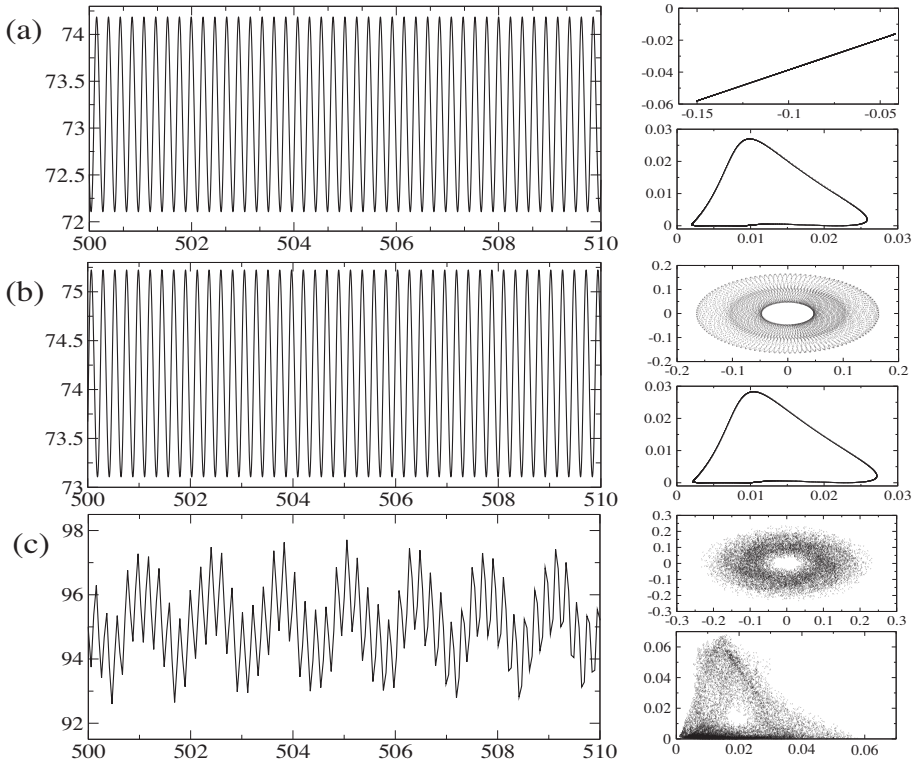

Fig. 6. Kinetic energy time series (left panel), projection of real and imaginary parts of the harmonic $\widehat{v}^x_{2,1,2}$ (upper right) and absolute value of two components of the same harmonic (bottom right) for (a) $R = 1780$, (b) $R = 1795$ and (c) $R = 2075$.

is identified when a projection of the harmonic is made in the laboratory frame (Fig. 6(b), upper right panel). From the bottom panel of the same figure it can be seen that QPA1 is in the same subspace as the PA. Recall from Fig. 5 that QPA1 is a traveling roll. Attractor QPA1 is "destroyed" (actually, it loses stability) in a global bifurcation called boundary crisis (Grebogi et al., 1987) at $R \approx 2055$, and a transient quasiperiodic behavior is observed for initial conditions in its region. Fig. 6(c) refers to another attractor that will be commented later.

For $1880 \leqslant R \leqslant 2070$ the attractor QPA1 coexists with a family of attractors named A1 in Fig. 4. For the branch A1, a sequence of quasiperiodic and chaotic regimes is observed, depending on R. For some ranges of R, the first two exponents are null (quasiperiodic attractors), whereas in some ranges the first exponent is positive (chaotic attractors). Windows of quasiperiodic behavior are seen between regions of chaotic states.

For $2073 \leqslant R \leqslant 2080$, a new chaotic attractor, ITMA, appears. The ITMA displays "on–off" intermittent switches between phases of quasiperiodic (on) and chaotic (off) behavior, (Fig. 7(a)). A close inspection of the state space during each phase reveals that this attractor is formed by a merging of A1 and the set resulting from the "destruction" of QPA1. A quasiperiodic phase of ITMA, for instance $t < 1750$, is identified as the destabilized QPA1 while the chaotic phases, e.g., $5000 \leqslant t \leqslant 5400$, as the destabilized A1. As an illustration, compare Fig. 7(b), that shows a portion of the time series for the chaotic phase of the ITMA at $R = 2073$, with the A1 time series for $R = 2070$ shown in Fig. 7(c). Projections of Fourier coefficients (not shown) were also made to verify the correspondence between the two kinds of phases of ITMA and the destabilized attractors QPA1 and A1. This scenario supports an interior crisis (Rempel et al., 2004) as the origin of ITMA due to the collision of A1 and the destabilized QPA1. The ITMA undergoes its own boundary crisis at $R \approx 2080$, where it is destroyed.

Another quasiperiodic attractor, QPA2, is found for $2075 \leqslant R \leqslant 2130$, where all three computed Lyapunov exponents vanish. Apparently, it bifurcates from the previously destabilized QPA1, since both have similar energy levels and phase space projections, as shown in Fig. 6(b) and (c). For $R = R_{HCA} \approx 2133$, QPA2 gives raise to a hyperchaotic attractor (HCA), with two positive Lyapunov exponents. Variation of the Lyapunov exponents with R for attractors QPA1, QPA2 and HCA is shown in Fig. 8. Note that a third positive Lyapunov exponent appears for HCA after $R \approx 2200$. The gap marked by the two vertical dotted lines indicates a region where the HCA is highly intermittent with switching between two phases with different Lyapunov exponents.

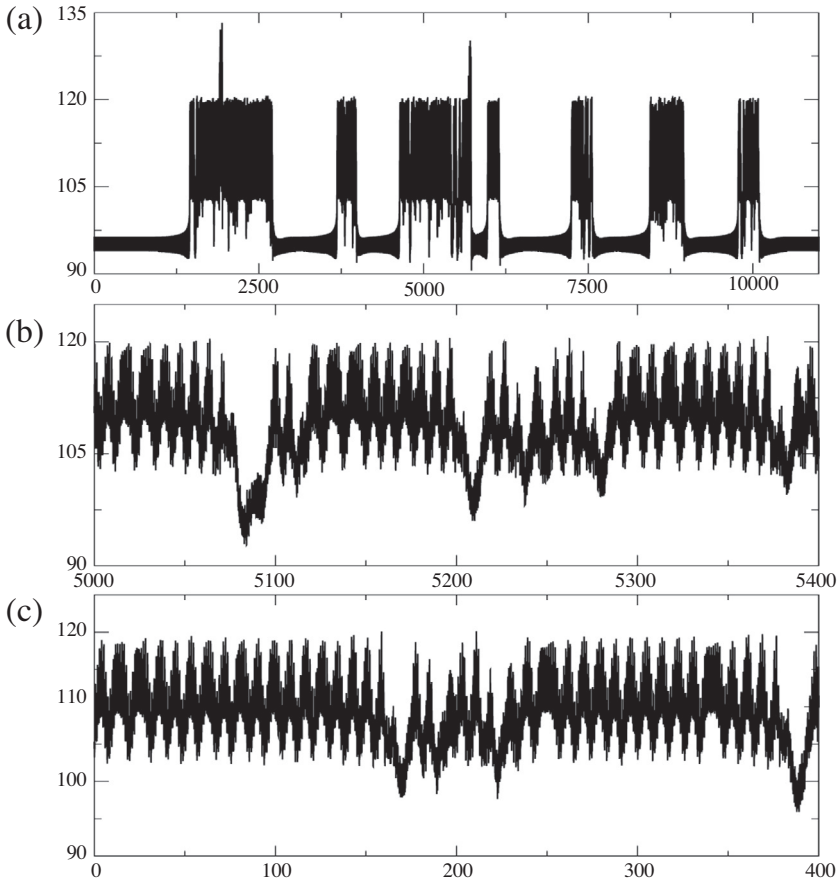

Fig. 7. Kinetic energy evolution for ITMA at $R = 2075$ (a) and a zoom in the chaotic phase for $5000 \leqslant t \leqslant 5400$ (b). In (c) the kinetic energy evolution for the A1 attractor at $R = 2070$ is presented. The ITMA presents two defined phases related to destabilized attractors QPA1 and A1.

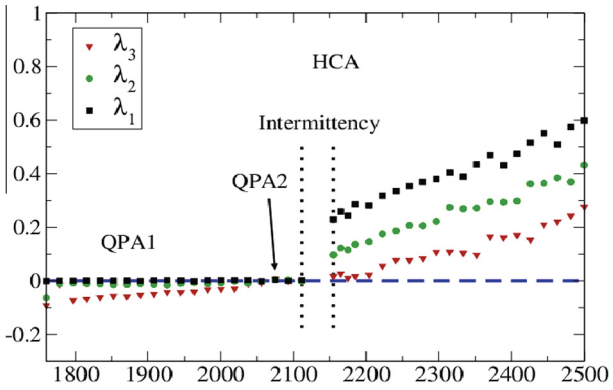

Fig. 8. The bifurcation diagram of the three largest Lyapunov exponents for $1760 \geqslant R \geqslant 2500$. The hyperchaotic attractor emerges from an interior crisis at $R = 2133$.

It may be odd to see a system discontinuously jumping from zero to two positive Lyapunov exponents as in R_{HCA}. However, one has to consider that only the Lyapunov exponents of the attracting states are being plotted. Recall that the destabilization of an attractor in a crisis always transforms a chaotic attractor into a chaotic transient. To illustrate this, Fig. 9 shows the time series and phase space trajectories as one decreases R using initial conditions from the HCA. Fig. 9(a) plots the HCA for $R = 2167$. Note the on–off intermittent switching between phases of small and high energy. For $R = 2130 < R_{HCA}$ (Fig. 9(b)), there is an initial hyperchaotic transient before the trajectory settles to QPA2. It is known that nonattracting chaotic sets called *chaotic saddles* (CS) are responsible for such chaotic transients (Rempel and Chian, 2007). A comparison between Fig. 9(a) and (b) indicates that the intermittent time series of HCA involves switching between CS and the destabilized QPA2 (red regions in Fig. 9(a)), which reveals that the transition from QPA2 (red region in Fig. 9(b)) to HCA occurs via an interior crisis in which QPA2 collides with the surrounding CS to form HCA. After the collision, the destabilized QPA2 becomes embedded in the enlarged chaotic attractor. Fig. 10(a)

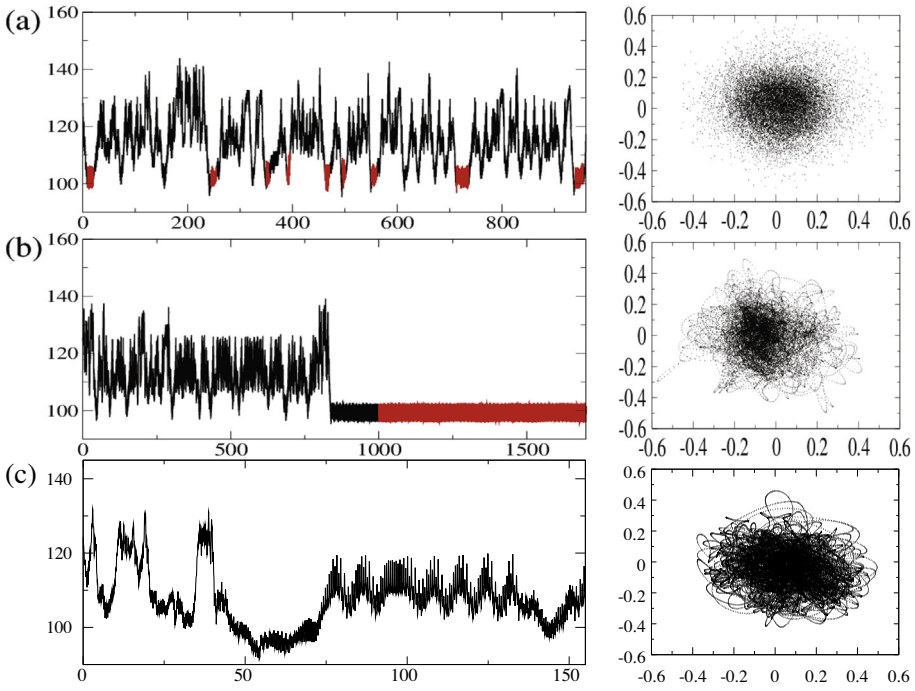

Fig. 9. Kinetic energy time series (left panels) and phase space projections (right panels) of the imaginary part (vertical axes) and real part (horizontal axes) of Fourier coefficient $\widehat{v}^{x}_{2,1,2}$ for the hyperchaotic attractor at $R = 2167$ (a), the chaotic transients for $R = 2130$ (b) and $R = 2070$ (c). Regions in red are compared in Fig. 10. (For interpretation of the references to color in this figure legend, the reader is referred to the web version of this article.)

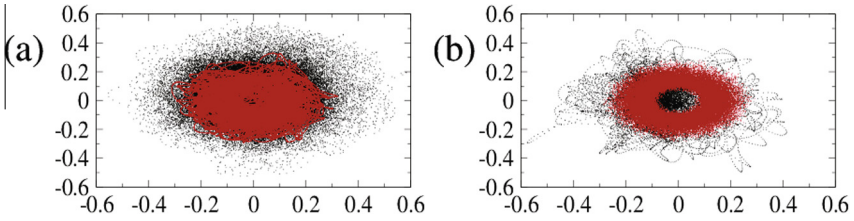

Fig. 10. Phase space projections of the imaginary part (vertical axes) and real part (horizontal axes) of the harmonic $\widehat{v}^{x}_{2,1,2}$ for the red regions of Fig. 9 for $R = 2167$ (a), and $R = 2130$ (b). (For interpretation of the references to color in this figure legend, the reader is referred to the web version of this article.)

shows the HCA (black dots) superposed by the destabilized QPA2 (red dots) for $R = 2167$. Fig. 10(b) shows the chaotic transient (black dots) and the stable QPA2 (red dots) for $R = 2130$.

The CS exists in the whole R interval between HCA and ITMA, and even prior to the formation of ITMA. Note in Fig. 9(c) that it is responsible for chaotic transients for $R = 2070$, where the trajectory eventually converges to A1. Thus, the dotted lines CS to the left and to the right of ITMA in Fig. 4. Although we have not computed the Lyapunov exponents of the CS due to its repelling nature which impairs the direct computation of long time averages, we conjecture that hyperchaos is first developed in this set prior to R_{HCA}.

4. Conclusions

4.1. Comparison with experimental observations and numerical results

Several of the bifurcations found in our model have been observed in experimental works with different setups. For instance, Gollub and Benson (1980) conducted laboratory experiments with water by varying the aspect ratio and Prandtl number ($P = 2.5$–5), finding routes to convective chaos through quasiperiodicity and period-doubling bifurcations of periodic states. Intermittency was observed in an experiment with $P = 130$ in Bergé et al. (1980).

Although we are unaware of other three-dimensional direct numerical simulations of R–B convection where a crisis leads to an intermittent route to hyperchaos, we note that there is remarkable similarity between our results and the ones previously reported by Paul et al. (2011) for a reduced two-dimensional model. For large Prandtl number ($P = 6.8$), they were able to detect a sequence of bifurcations as a function of R that leads to steady rolls, traveling waves, order-chaos-order transitions, multistability, quasiperiodic phase-locking route to chaos, as well as an attractor-merging crisis and hyperchaos.

4.2. General conclusions

We have presented results of a study of transition to spatiotemporal chaos in R–B convection, where a route to hyperchaos through intermittency is reported. Two coexisting steady solutions undergo independent bifurcations (including Hopf, phase locking and crises) before they are merged into a single intermittent attractor with a positive Lyapunov exponent, indicating chaos. As the Rayleigh number is increased, a second, then a third Lyapunov exponents become positive.

Note the similarity between this route to hyperchaos and the one reported by Clerc and Verschueren (2013), where a quasiperiodic route to hyperchaos is found in the Lifshitz normal form, a nonvariational generalization of the Swift–Hohenberg equation, which describes stationing patterns in Rayleigh–Bénard convection. In our case, there is the presence of an interior crisis after the appearance of the second incommensurate frequency. As a direct consequence of this crisis, on–off intermittency is observed in the time series of the kinetic energy. This dynamic phenomenon takes place whenever trajectories can temporally escape from a region of the phase space responsible for the coherent "on" phases, and wander in its vicinity for some time ("off" phase), before they are reinjected in the "on" region. This phenomenon has been detected in numerical simulations of long waves with applications to tsunamis (Chian et al., 2010; Toledo et al., 2013), keplerian shear flows with applications to accretion disks (Miranda et al., 2015) and nonlinear dynamos with applications to the solar cycle (Rempel et al., 2009; Spiegel, 2009).

As mentioned before, the mechanisms of formation, deformation and destruction of convective cells are also important for magnetic field amplification, since in highly conducting magnetized fluids, convective layers deform the lines of force and drag them to the boundaries between different convective cells, where the field grows (Weiss, 1966; Chian et al., 2014). Thus, as a follow up of the present work, we intend to study bifurcations in convection in the presence of magnetic fields, as well as magnetic field and rotation.

Acknowledgements

EVC acknowledges financial support from CAPES. RC and ELR acknowledge financial support from FAPESP (Grants 2013/01242-8 and 2013/22314-7, respectively). ELR also acknowledges financial support from CNPq (Brazil, Grant 305540/2014-9).

References

Alligood, K.T., Sauer, T.D., Yorke, J.A., Crawford, J.D., 1997. Chaos: An Introduction to Dynamical Systems. Springer-Verlag, New York.

Bénard, H., 1901. Les tourbillons cellulaires dans une nappe liquide - méthodes optiques d'observation et d'enregistrement (Cell vortices in a liquid sheet – optical observation and recording methods). J. Phys. Théor. Appl. 10, 254–266.

Bergé, P., Dubois, M., Manneville, P., Pomeau, Y., 1980. Intermittency in RayleighBénard convection. J. Phys. Lett. 41, 341–345.

Bodenschatz, E., Pesch, W., Ahlers, G., 2000. Recent developments in Rayleigh–Bénard convection. Annu. Rev. Fluid Mech. 32, 709–778.

Boyd, J.P., 2000. Chebyshev and Fourier Spectral Methods. Dover Publications, New York.

Brandenburg, A., Subramanian, K., 2005. Astrophysical magnetic fields and nonlinear dynamo theory. Phys. Rep. 417, 1–209.

Chandrasekhar, S., 1961. Hydrodynamic and Hydromagnetic Stability. Dover Publications, New York.

Chian, A.C.-L., Kamide, Y. (Eds.), 2007. Handbook of the Solar-Terrestrial Environment. Springer, New York.

Chian, A.C.-L., Miranda, R.A., Rempel, E.L., Yamada, M., Saiki, Y., 2010. Amplitude-Phase Synchronization at the Onset of Permanent Spatiotemporal Chaos. Phys. Rev. Lett. 104, 254102.

Chian, A.C.-L., Rempel, E.L., Aulanier, G., Schmieder, B., Shadden, S. C., Welsch, B.T., Yeates, A.R., 2014. Detection of coherent structures in photospheric turbulent flows. Astrophys. J. 786, 51.

Childress, S., Gilbert, A.D., 1995. Strecth, Twist, Fold: The Fast Dynamo. Springer-Verlag, Berlin.

Clerc, M.G., Verschueren, N., 2013. Quasiperiodicity route to spatiotemporal chaos in one-dimensional pattern-forming systems. Phys. Rev. E 88, 052986.
Cox, S.M., Matthews, P.C., 2002. Exponential time differencing for stiff systems. J. Comput. Phys. 176, 430–455.
Cross, M.C., Hohenberg, P.C., 1993. Pattern formation outside of equilibrium. Rev. Mod. Phys. 65, 851–1112.
Egolf, D.A., Melnikov, I.V., Pesch, W., Ecke, R.E., 2000. Mechanisms of extensive spatiotemporal chaos in Rayleigh–Bénard convection. Nature 404, 733–736.
Fearn, D., Roberts, P., 2007. The Geodynamo. CRC Press, Roca Baton.
Fowler, C.M.R., 2005. The Solid Earth: An Introduction to Global Geophysics. Cambridge, Cambridge.
Getling, A.V., 1998. Rayleigh–Bénard Convection: Structures and Dynamics. World Scientific, Singapore.
Gollub, J.P., Benson, S.V., 1980. Many routes to turbulent convection. J. Fluid Mech. 100, 449–470.
Grebogi, C., Ott, E., Romeiras, F., Yorke, J.A., 1987. Critical exponents for crisis-induced intermittency. Phys. Rev. A 36, 5365–5380.
Hramov, Alexander E., Koronovskii, Alexey A., Maximenko, Vladimir A., Moskalenko, Olga I., 2012. Computation of the spectrum of spatial Lyapunov exponents for the spatially extended beam-plasma systems and electron-wave devices. Phys. Plasmas 19, 082302.
Kapitaniak, T., Maistrenko, Y., Popovych, S., 2000. Chaos-hyperchaos transition. Phys. Rev. E 26, 1792–1976.
Karimi, A., Paul, M.R., 2012. Quantifying spatiotemporal chaos in Rayleigh–Bénard convection. Phys. Rev. E 85, 046201.
Lorenz, E.N., 1963. Deterministic nonperiodic flow. J. Atmos. Sci. 20, 130–141.
Macek, W.M., Strumik, M., 2014. Hyperchaotic intermittent convection in a magnetized viscous fluid. Phys. Rev. Lett. 112, 074502.
Miranda, R.A., Rempel, E.L., Chian, A.C.-L., 2015. On-off intermittency and amplitude-phase synchronization in Keplerian shear flows. MNRAS 448, 804–813.
Olson, P., 2007. In: Overview in Treatise on Geophysics. In: Schubert, G. (Ed.), . Core Dynamics, vol. 8. Elsevier, Amsterdam, pp. 1–30.
Paul, M.R., Einarsson, M.I., Fischer, P.F., Cross, M.C., 2007. Extensive chaos in Rayleigh–Bénard convection. Phys. Rev. E 75, 045203(R).
Paul, S., Wahi, P., Verma, M.K., 2011. Bifurcations and chaos in large-Prandtl number Rayleigh–Bénard convection. Int. J. Non-Linear Mech. 46, 772–781.
Podvigina, O.M., 2006. Magnetic field generation by convective flows in a plane layer. Eur. Phys. J. B 50, 639–652.
Podvigina, O.M., 2008. Magnetic field generation by convective flows in a plane layer: the dependence on the Prandtl numbers. Geophys. Astrophys. Fluid Dyn. 102, 409–433.
Rempel, E.L., Chian, A.C.-L., 2007. Origin of transient and intermittent dynamics in spatiotemporal chaotic systems. Phys. Rev. Lett. 28, 014101.
Rempel, E.L., Chian, A.C.-L., Macau, E.E.N., Rosa, R.R., 2004. Analysis of chaotic saddles in low-dimensional dynamical systems: the derivative nonlinear Schrödinger equation. Physica D 199, 407–424.
Rempel, E.L., Proctor, M.R.E., Chian, A.C.-L., 2009. A novel type of intermittency in a non-linear dynamo in a compressible flow. MNRAS 400, 509–517.
Rössler, O.E., 1979. An equation for hyperchaos. Phys. Lett. A 71, 155–157.
Rüdiger, G., Hollerbach, R., 2004. The Magnetic Universe: Geophysical and Astrophysical Dynamo Theory. Wiley-VCH, Weinheim.
Spiegel, E.A., 2009. Chaos and intermittency in the solar cycle. Space Sci. Rev. 144, 25–51.
Toledo, B.A., Chian, A.C.-L., Rempel, E.L., Miranda, R.A., Muñoz, P. R., 2013. Wavelet-based multifractal analysis of nonlinear time series: The earthquake-driven tsunami of 27 February 2010 in Chile. Phys. Rev. E 87, 022821.
Weiss, N.O., 1966. The expulsion of magnetic flux by eddies. Proc. R. Soc. A 293, 310–328.
Zhou, Q., Chen, Z.-Q., Yuan, Z.-Z., 2008. Hyperchaos–chaos–hyperchaos transition in a class of on-off intermittent systems driven by a family of generalized Lorenz systems. Chin. Phys. Lett. 25, 3169–3172.